The practical consequence of the first observation is that the present data set is inadequate to address the important question of possible defocusing and resultant degradation (*8*) of Seasat SAR imagery of azimuth-traveling waves, for most waves were apparently traveling in a direction that was within 45° of the satellite range coordinate. This is so because the wave climatology during September for the region in the Gulf of Alaska corresponding to the imagery examined is such that most wave energy can be expected to propagate toward 90° (*9*) while the satellite heading at these latitudes was about 330°.

Despite these limitations on the data, some tentative conclusions can be drawn. There are 11 Seasat SAR/surface-aircraft data pairs in Table 3 which were acquired within 25 km and 1.5 hours of each other; this set yields agreement in wavelength to within about ± 15 percent and agreement in wave direction to within about ± 25°. Thus, the limited data set examined so far meets NOAA requirements for oceanographic measurement accuracy of ± 10 to ± 25 percent in wavelength and ± 10° to ± 30° in wave direction (*10*). If data pairs taken more than 25 km apart are included in the comparison, the agreement in wavelength is degraded to about ± 25 percent.

The data in Tables 1 and 2 also suggest a range of 1 to 2 m for $H_{1/3}$ where the lower limit for wave detection might fall. Thus, no waves were detected in Seasat SAR imagery acquired during revolution 1306, for which P-R buoy measurements indicated an $H_{1/3}$ of about 1 m; however, waves were detected during revolution 1126, for which an $H_{1/3}$ of about 2 m was observed. However, Tables 1 and 2 show that the dominant ocean wavelength and the relative angles between wind, wave, and satellite headings differed significantly in each case; these parameters may be equally as important as $H_{1/3}$ relative to wave detection capabilities. Thus caution must be exercised in the interpretation of this result.

Most of the GOASEX SAR data and surface measurements remain to be compared and analyzed. The preliminary nature of the data reduction, comparison, and analysis of the limited data set examined here should be noted. Seasat imagery of improved quality will be used in later analyses. The P-R buoy data will be processed at finer frequency resolution, and the resulting spectra transformed to wave number or wavelength space to improve comparisons with intensity spectra resulting from OFT's of Seasat imagery. Aircraft data will be digitized, so that geometric corrections and motion compensations can be made more accurately.

F. I. GONZALEZ
Pacific Marine Environmental Laboratory, National Oceanic and Atmospheric Administration, Seattle, Washington 98105

R. C. BEAL
Applied Physics Laboratory, Johns Hopkins University, Laurel, Maryland 20810

W. E. BROWN
Jet Propulsion Laboratory, California Institute of Technology, Pasadena 91103

P. S. DELEONIBUS, J. W. SHERMAN III
National Environmental Satellite Service, National Oceanic and Atmospheric Administration, Washington, D.C. 20233

J. F. R. GOWER
Institute of Ocean Sciences, Sidney, British Columbia, Canada V8L 4V2

D. LICHY
U.S. Army Corps of Engineers, Coastal Engineering Research Center, Fort Belvoir, Virginia 22060

D. B. ROSS
Sea-Air Interaction Laboratory, National Oceanic and Atmospheric Administration, Miami, Florida 33149

C. L. RUFENACH
Wave Propagation Laboratory, National Oceanic and Atmospheric Administration, Boulder, Colorado 80303

R. A. SHUCHMAN
Environmental Research Institute of Michigan, Ann Arbor 48107

References and Notes

1. W. E. Brown, Jr., C. Elachi, T. W. Thompson, *J. Geophys. Res.* **81**, 647 (1976); C. Elachi and W. E. Brown, *IEEE Trans. Antennas Propag.* **AP-25**, 84 (1977); T. R. Larson, L. I. Moskowitz, J. W. Wright, *ibid.* **AP-24**, 393 (1976); J. W. Wright, *ibid.* **AP-14**, 719 (1966); P. G. Teleki, R. A. Shuchman, W. E. Brown, Jr., W. McLeish, D. E. Ross, M. Mattie, *Proceedings of the Oceans '78 Conference* (Washington, D.C., 6 to 8 September 1978), pp. 639-648.
2. R. A. Shuchman, E. S. Kasischke, A. Klooster, *Synthetic Aperture Radar Ocean Wave Studies* (Final Report 131700-3-F, Environmental Research Institute of Michigan, Ann Arbor, 1978).
3. J. W. Goodman, *Introduction to Fourier Optics* (McGraw-Hill, New York, 1968).
4. G. H. Born, D. B. Lame, J. C. Wilkerson, Eds. "GOASEX Workshop Report" (Report 622-101, Jet Propulsion Laboratory, California Institute of Technology, Pasadena, 1979) (internal document), vol. 1, appendix A.
5. J. A. Ewing, *J. Mar Res.* **27**, 163 (1969); H. Mitsuyasu, F. Tasai, T. Suhara, S. Mizumo, L. Ohkusu, T. Honda, K. Rikiishi, *J Phys. Oceanog.* **5**, 750 (1975).
6. W. C. Chiu, *Am. J. Phys.* **35**, 642 (1967).
7. R. K. Raney, paper presented at the 5th Canadian Remote Sensing Symposium, Victoria, British Columbia, 1978.
8. R. A. Shuchman and J. S. Zelenka, *Boundary-Layer Meteorol.* **13**, 181 (1978); A. Jain, *J. Appl. Phys.* **15**, 323 (1973).
9. U.S. Navy, *U.S. Navy Marine Climatic Atlas of the World*, vol. 2, *North Pacific Ocean* (Naval Air Force Document 50-1C-529, Naval Weather Service Detachment, Asheville, N.C., 1977), p. 265.
10. "NOAA Program Development Plan for Seasat-A: Research and Applications" (Report NOAA-S/T 77-2574, Department of Commerce, Washington, D.C., March 1977), p. 1-2.
11. We thank J. C. Dwyer of the Environmental Research Institute of Michigan (ERIM) and T. Bicknell of the Jet Propulsion Laboratory for providing the optical Fourier transforms. We thank P. G. Teleki and J. Dunne for their advice and helpful comments during and after the GOASEX Workshop. The ERIM portion of the analysis was supported under NOAA National Environmental Satellite Service contract MO-AO1-78-00-4339. Portions of the research described in this report were carried out by the Jet Propulsion Laboratory, California Institute of Technology, and were sponsored by the National Oceanic and Atmospheric Administration and National Aeronautics and Space Administration.

20 April 1979

Seasat Visible and Infrared Radiometer

Abstract. *Visual and infrared images produced by the Seasat visible and infrared radiometer (VIRR) are adequate for the identification of cloud, land, and water features. A statistical comparison of VIRR-derived sea-surface temperatures in a cloud-free region with a National Oceanic and Atmospheric Administration analysis based on various surface measurements taken in the same region showed agreement to ± 1.7°K root-mean-square.*

The visible and infrared radiometer (VIRR), a supporting instrument system on Seasat, has as its principal function to provide images of visual reflection and thermal infrared emission from ocean, coastal, and atmospheric features that can aid in interpreting the data from the other Seasat sensors. The VIRR is also expected to provide some derived quantitative measurements of such factors as sea-surface temperature and cloud-top height.

All the instruments on-board Seasat except the VIRR are microwave systems, active or passive, but only one other instrument in addition to the VIRR, the synthetic aperture radar (SAR), is an imaging system. The VIRR will provide images encompassing the data swaths of all the other Seasat sensors, with a ground resolution equal to or greater than that of any other Seasat sensor except the SAR and the radar altimeter. Thus, investigators can determine whether the field of view of their instrument is partly or completely filled by cloud, determine something about the cloud type and height, confirm the presence or absence of land, and possibly detect ocean thermal fronts.

The VIRR is a surplus scanning radiometer (SR) originally built for the improved TIROS (Television Infrared Operational Satellite) series, whose operating altitude is about twice that of Seasat. Principally because of the data rate limitations, the images generated from the VIRR are degraded twofold in the infrared (IR) and fourfold in the visible (VIS) with respect to the full capability of the instrument operating in a lower orbit. On-board digitization of VIRR data is expected to improve the performance of the VIRR over that of the earlier SR.

One channel of this instrument operates in the VIS region of the spectrum, the other in a spectral region of atmospheric transmission in the IR. Scanning is accomplished by means of a rotating mirror mounted at 45° to the optical axis of the collecting telescope. The mirror rotates continuously, creating a line scan perpendicular to the orbital motion of the spacecraft. The motion of the spacecraft provides the second dimension of scan. The scan rate for earlier satellites was such that the satellite's ground motion at nadir was equal to one resolution element, thus creating a raster with each scan line adjacent to the earlier one. In the case of the VIRR, the radiometer was originally designed to operate at a higher altitude than that of Seasat; consequently, there is a gap between scan lines at nadir of just under one resolution element.

The radiation from the earth is reflected from the scan mirror to a Cassegrain-type telescope 12.5 cm in diameter that focuses the radiation to a field stop, which defines the angular spatial resolution. A relay optical system that transmits the radiation to a dichroic beamsplitter, which separates it into the short and long wavelengths. The VIS energy is then focused onto a silicon photodiode and the IR onto a thermistor bolometer. Table 1 lists some of the important parameters of the instrument. The electrical signals from the detectors are then amplified, demodulated, and digitized to 8-bit accuracy for transmission to the ground. The portions of the scan that are sampled are the earth scan (from ± 51.6° of nadir) containing the 224 pixels of VIS and 224 pixels of IR information, the space (cold reference) view, and internal housing (warm reference) view that are used for in-flight calibration. A five-step

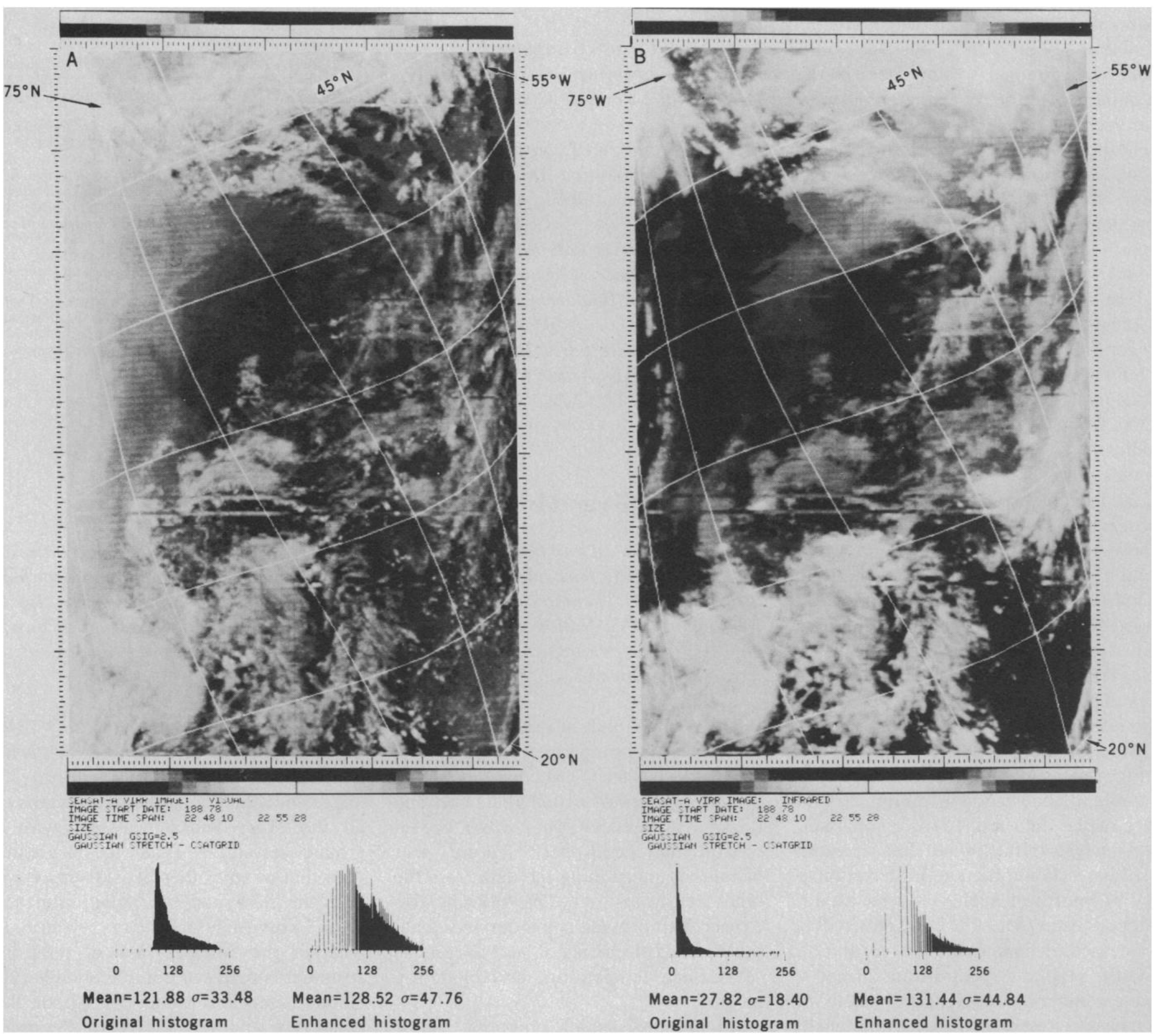

Fig. 1. (A) Seasat-A VIRR visual image of the western North Atlantic. (B) Seasat-A VIRR infrared image of the western North Atlantic. Both images were obtained simultaneously on 7 July 1978 at approximately 22:51:00 G.M.T.

Table 1. Some VIRR instrument parameters; NE, noise equivalent.

Channel	Resolution: Angular (mrad)	Resolution: Ground (nadir) (km)	Spectral region (μm)	Sensitivity (NE differential)	Temperature* (NEΔT)	Dynamic range
Visible	2.8	2.3†	0.49 to 0.94	Not applicable		65 to 10,000 foot-lamberts (scene brightness)
Infrared	5.3	4.4†	10.5 to 12.5	Accurate to 1.5°K with a scene at 185°K	Accurate to 0.27°K with a scene at 300°K	180° to 330°K (scene temperature)

*Instrument temperature is 25°C. †Effective resolution of the digital data received on the ground is 6.2 km cross-track and 8.3 km along-track for both channels.

voltage staircase is incorporated into each scan line's content to correct for digitizing and transmission nonlinearities of the system.

In order to evaluate the ability of the VIRR to meet the goals listed in the first paragraph of this report, a number of cloud-free or nearly cloud-free ocean areas were selected from Seasat passes over the western North Atlantic, eastern North Pacific, and Gulf of Mexico on 7, 8, 9, 10, and 11 July 1978. The newly developed master sensor data record catalog search software in the Jet Propulsion Laboratory's (JPL) algorithm development facility (ADF) was useful in this selection. The determination of cloud-free conditions was aided by inspection of VIS and IR images (2-km resolution) from the National Oceanic and Atmospheric Administration (NOAA) Geostationary Operational Environmental Satellite. Cases were selected in which VIRR VIS images were available; however, in all cases it was near sunset local time, and illumination tended to be poor on the eastern side of the VIRR data swath.

The image-processing laboratory at the JPL produced the gridded visual image (Fig. 1A) for revolution 156, day 188 (7 July 1978). The data for this image were taken directly from a VIRR sensor data record (SDR) (that is, raw, noncalibrated data). The original histogram (bottom left) shows the distribution of brightnesses in the original data, which are highly skewed toward the dark end because of a very low sun (in the west). The extreme redistribution of brightnesses in this greatly enhanced VIS image is shown in the enhanced histogram (bottom right). The result of this enhancement is to generally saturate the scene on the western (left) edge of the swath; to enhance cloud shadows, particularly in the eastern (right) half of the image; and to produce what appear to be contours of sun glitter to the west of nadir in the cloud-free region of the ocean east of the northeastern United States. A few isolated noise stripes are evident parallel to the scan lines; for example, near scan line divisions 89 and 92, counting from the top.

The format of the IR image (Fig. 1B) is the same as that of the corresponding VIS image. The same noise stripes appear as in the VIS. The warmer the radiating surface, the darker the tone in the image. The warmer land is thus darker than the adjacent cooler ocean. The east coast of the United States from near Cape Hatteras to north of Cape Cod is clearly visible, as are the cooler waters of Lake Ontario and Lake Erie and the warm waters of the north wall of the Gulf Stream (mixed with clouds). Lower clouds, which are warmer than higher clouds, appear in intermediate gray shades, whereas the highest cloud tops appear in the brightest tones.

Time and other constraints limited the detailed geophysical evaluation of digital VIRR data to IR samples from a large cloud-free ocean area just off the east coast of the United States between about 35°N and 40°N and out to 65°W on 7 July 1978. Approximately every seventh pixel from every fifth scan line was used. When cloud- and land-contaminated pixels were omitted, a total sample of 139 pixels remained for analysis and comparison with surface truth. Another sample of 14 successive pixels on four adjacent scan lines (N = 56) was selected from a region with a low temperature gradient of this same cloud-free area for a noise-level evaluation.

One of the first steps in the geophysical evaluation was to cross-check the scan line and pixel arrays as portrayed graphically in the IR and VIS images produced directly from VIRR SDR's with the corresponding measurements given in the digital printout, which is produced from the Interim Geophysical Data Record (IGDR) tape. This IGDR tape is produced when VIRR SDR's are processed through a set of VIRR-specific processing algorithms housed in the JPL's Seasat ADF. There is excellent agreement between the location of features with high thermal contrast (for example, coastline, Gulf Stream, cloud edges) and appropriate gradients in the digital profile; the overall noise levels in these data appear very low.

There is a substantial lowering of the brightness temperature at wavelengths of 10.5 to 12.5 μm as a result of water vapor in the atmospheric path; therefore, to obtain an adequate estimate of the physical temperature of the earth's surface or of low cloud tops requires an atmospheric correction. The best correction is based on a vertical profile of water vapor from radiosondes or water vapor

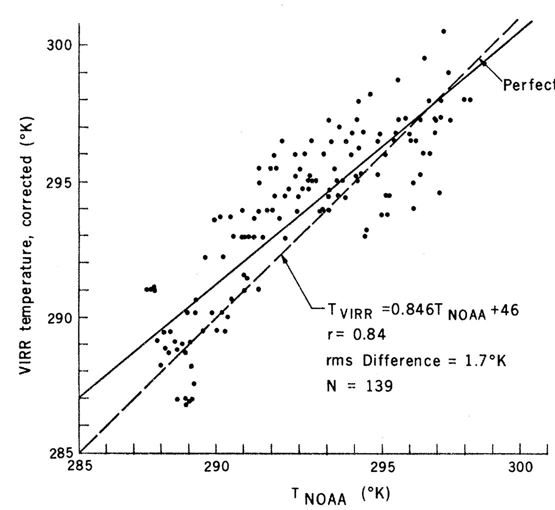

Fig. 2. Scatter diagram of Seasat-A VIRR-derived surface temperatures, corrected for atmospheric attenuation, versus NOAA temperature field estimates for the same locations. The VIRR data were obtained at approximately 22:51:00 G.M.T. on 7 July 1978; the NOAA field is for the time period between 5 July and 10 July 1978.

information from the Seasat scanning multichannel microwave radiometer (SMMR). As none of these was available for this evaluation, an empirical correction, which is a function of brightness temperature itself, was used. The correction values are based on theoretical calculations and a large number of model atmospheres, and they are generally accurate to only about ± 20 percent.

Some of the results of this initial geophysical evaluation are illustrated in a plot (Fig. 2) of the 139-sample VIRR surface temperature estimates versus the NOAA surface field temperatures interpolated at the same pixel locations; the perfect fit line (slope of unity) and the least-squares linear regression line are shown. The linear regression correlation coefficient, $r = 0.84$, and the root-mean-square difference (or standard error of the estimate) of 1.7°K represent excellent agreement in view of the uncertainty in the atmospheric correction and the uncertainty and the smoothness of the NOAA field. The means of the two sets of temperatures were 293.9°K (VIRR) and 293.1°K (NOAA), and the respective standard deviations were 3.21° and 3.2°K.

We estimated the noise level of the IR data by using a sample of 14 successive pixels on four successive scan lines in an area of relatively low thermal gradient. The standard deviation of all 56 sample pixels from the sample mean of 283.35°K is 0.54°K. When this calculation is repeated with the pixel-to-pixel differences (along with each scan line), the mean difference is −0.04°K and the standard deviation is 0.57°K.

E. PAUL McCLAIN
National Environmental Satellite Service, National Oceanic and Atmospheric Administration, Washington, D.C. 20233

RICHARD A. MARKS
Jet Propulsion Laboratory, California Institute of Technology, Pasadena 91103

Note

1. The research described in this report was carried out by the Jet Propulsion Laboratory, California Institute of Technology, under NASA contract NAS7-100.

20 April 1979

Venus: Further Evidence of Impact Cratering and Tectonic Activity from Radar Observations

Abstract. *Earth-based radar images at a resolution of 10 kilometers show a diverse surface terrain on Venus, probably produced by both impact events and tectonic activity. Only a small number of craters of apparent impact origin are seen. Large-scale features show lineaments and parallel ridges suggesting tectonic origins.*

On 20 June 1972, Rumsey *et al.* (*1*), using the Jet Propulsion Laboratory–NASA (JPL-NASA) planetary radar system, obtained both an image and an altitude map of a small area surrounding the sub-Earth point on Venus for that day. This image, which was at a resolution (*2*) of approximately 10 km, showed what appeared to be a crater 160 km in diameter, the first reasonably unambiguous identification of a small feature on the surface of the planet. Since that time Goldstein *et al.* (*3, 4*), using the JPL-NASA system, have produced images and altitude maps of a number of regions near the equator, while Campbell *et al.* (*5*), using the radar system at the Arecibo Observatory, have produced an image covering a large area at high northern latitudes. These images show a diversified surface. Evident are a number of small and large roughly circular structures, a 1000-km-long trough, numerous isolated peaks, and a number of large irregularly shaped areas of high surface roughness. On the basis of gross morphology and size distribution, Saunders and Malin (*6*) suggested that a group of these circular features in one region may be impact craters while two others may be volcanic constructs. The 1000-km-long trough they interpret in terms of a rift valley. This report presents a number of new images which support the suggestion that the surface of Venus shows a history of both impact events and tectonic activity.

Venus was mapped with the Arecibo 12.5 cm wavelength radar in 1975 and 1977. The 1975 observations were limited to relatively high latitudes and to resolutions larger than 10 km, while the 1977 observations concentrated on the lower latitudes and achieved resolutions down to 5 km over a few regions. Combining the images from the 2 years will give coverage of most of the area between longitudes 270° and 20° and from latitude 60°S to 70°N. A strip from roughly 10°S to 10°N will be either missing or of poor quality.

Figures 1 through 3 are images in a Mercator projection (*7*) covering regions in the vicinity of the first two features discovered on the surface of the planet in 1962 (*8*) and tentatively named Alpha and Beta at that time. For all these images the average scattering properties of the planet have been removed (*9*) so that one sees the ratio between the received power from a particular area and that expected for a homogeneous surface having the same average properties as are observed for Venus. Increasing brightness corresponds to increasing levels of power backscattered toward the radar per unit surface area on the planet. In general, most brightness differences are due either to changes in the average slope of the surface over the resolution cell so that the effective incidence angle (θ) is changed or to differences in the degree of small-scale surface roughness (on the order of the wavelength of the incident radiation). At incidence angles below about 15° the scattering law [see (*9*)] is very sensitive to changes in the average slope. Good examples of this are crater walls, mountainsides, and so on. At angles above 30° most contrast changes appear to be determined by differences in small-scale surface roughness. The greater the roughness, the brighter the reflection. In theory, changes in the dielectric constant of the surface material due to differences in composition, or in compactness for powdered surfaces, should be discernible, but generally these seem to be masked by changes in the surface roughness. At the intermediate angles between about 15° and 30° contrast differences may be due to changes in either the average slope or the small-scale surface roughness, but they tend to be rather small.

Although a number of "craterlike" and "basinlike" formations can be seen in the images, most of the regions of high reflectivity have rather amorphous shapes. This situation is exemplified by the region in the vicinity of the feature Alpha shown in Fig. 1a. The whole southern part of this image is dominated by irregularly shaped areas of rough terrain. Most of them tend to be rather elongated and some are more than 1000 km in extent. It should be emphasized that while the enhancement of the backscattered signal is probably due to an increase in the small-scale roughness, this may be associated with changes in surface roughness on very much larger scales. Alpha is the bright region approximately 1300 km in diameter toward the upper right (east) in Fig. 1a. Just south of Alpha is a circular feature 280 km in diameter with a prominent central bright